Ededet A. Eno, Hitler Louis*, Tomsmith O. Unimuke, ThankGod C. Egemonye, Stephen A. Adalikwu, John A. Agwupuye, Diana O. Odey, Abu Solomon Abu, Ishegbe J. Eko, Chukwudubem E. Ifeatu and Tabe N. Ntui

Synthesis, characterization, and theoretical investigation of 4-chloro-6(phenylamino)-1,3,5-triazin-2-yl)asmino-4-(2,4-dichlorophenyl)thiazol-5-yl-diazenyl) phenyl as potential SARS-CoV-2 agent

Abstract: The synthesis of 4-chloro-6(phenylamino)-1,3,5-triazin-2-yl)amino-4-(2,4 dichlorophenyl)thiazol-5-yl-diazenyl)phenyl is reported in this work with a detailed structural and molecular docking study on two SARS-COV-2 proteins: 3TNT and 6LU7. The studied compound has been synthesized by the condensation of cyanuric chloride with aniline and characterized with various spectroscopic techniques. The experimentally obtained spectroscopic data has been compared with theoretical calculated results achieved using high-level density functional theory (DFT) method. Stability, nature of bonding, and reactivity of the studied compound was evaluated at DFT/B3LYP/6-31 + (d) level of theory. Hyper-conjugative interaction persisting within the molecules which accounts for the bio-activity of the compound was evaluated from natural bond orbital (NBO) analysis. Adsorption, Distribution, Metabolism, Excretion

***Corresponding author: Hitler Louis,** Computational and Bio-Simulation Research Group, University of Calabar, Calabar, Nigeria; and Department of Pure and Applied Chemistry, Faculty of Physical Sciences, University of Calabar, Calabar, Nigeria, E-mail: louismuzong@gmail.com

Ededet A. Eno, Tomsmith O. Unimuke, ThankGod C. Egemonye and John A. Agwupuye, Computational and Bio-Simulation Research Group, University of Calabar, Calabar, Nigeria; and Department of Pure and Applied Chemistry, Faculty of Physical Sciences, University of Calabar, Calabar, Nigeria

Stephen A. Adalikwu and Chukwudubem E. Ifeatu, Computational and Bio-Simulation Research Group, University of Calabar, Calabar, Nigeria

Diana O. Odey, Computational and Bio-Simulation Research Group, University of Calabar, Calabar, Nigeria; and Department of Biochemistry, Faculty of Physical Sciences, Cross River University of Technology, Calabar, Nigeria

Abu Solomon Abu, Computational and Bio-Simulation Research Group, University of Calabar, Calabar, Nigeria; and Department of Marine Biology, Faculty of Biology Sciences, University of Calabar, Calabar, Nigeria

Ishegbe J. Eko, Department of Polymer and Textile Engineering, Ahmadu Bello University Zaria, Kaduna, Nigeria

Tabe N. Ntui, Computational and Bio-Simulation Research Group, University of Calabar, Calabar, Nigeria; and Department of Chemistry, Faculty of Physical Sciences, Cross River University of Technology, Calabar, Nigeria

https://doi.org/10.1515/psr-2021-0161

and Toxicity (ADMET) properties of the experimentally synthesized compound was studied to evaluate the pharmacological as well as *in silico* molecular docking against SARS-CoV-2 receptors. The molecular docking result revealed that the investigated compound exhibited binding affinity of −9.3 and −8.8 for protein 3TNT and 6LU7 respectively. In conclusion, protein 3TNT with the best binding affinity for the ligand is the most suitable for treatment of SARS-CoV-2.

Keywords: ADMET; DFT; docking; synthesis; thiazole.

1 Introduction

Thiazoles are heterocyclic compounds containing sulfur and nitrogen atom. In pharmaceutical, several bioactive materials have been made with Thiazole as starting material [1]. However, several studies have reported possible germicidal [2, 3], analgetic [4], anti-inflammatory [5], anticonvulsant [6], cardiotonic [7], anticancer [8–10], antitubercular [11] and anthelmintic [12] effect of thiazoles. The significance of the thiazole moiety is largely attributed to its utilization as an active ingredient in various pharmaceutical products [13].

Recently, Thiazole derivative with phenylamino-1,3,5-triazine backbone has gained full attention as new nonsteroidal progesterone receptor (PR) antagonists which is of great importance in several physiological systems, most especially in the case of the female reproductive system [14]. In a study, the synthesis of 14 derivatives of 2-phenylamino-thiazole as an antimicrobial agent was conducted using Hantzsch reaction. The resulting 14 structures were later screened in order to verify their antimicrobial effect against two Gram-positive, one Gram-negative bacterial strains, and two fungal strains [15]. Also, DFT study was conducted on a novel 2-amino-4-(4-chlorophenyl) thiazole derivatives. The result reflects that the investigated compound demonstrated moderate anti-bacterial effect against *Staphylococcus aureus* and *Bacillus subtilis* and also high anti-fungal action against *candida Glabrata and Candida albicans* [16]. In another work, four novel derivatives of *3-(2-(3-Phenyl-5-substituted phenyl-4,5-dihydropyrazol-1-yl)thiazol-4-yl)-2H-chromen-2-one* named 1–4 were synthesized and characterized via spectroscopic methods. All the compounds involved were screened to ascertain their use as a bio-active material (acetyl cholinesterase inhibition potential). Among the studied compounds, compound 3 was the most effective as conducted in the acetyl cholinesterase (AChE) inhibition assay having IC50 of 27.29 μM. Molecular docking was also carried out on the compounds. The results obtained from the docking showed a strong relationship with their binding energies and the *in vitro* AChE inhibition assay [17].

Molecular docking is a crucial computational technique that has gained popularity over time, especially in drug discovery research, where it is used to model the

interaction between a ligand and a protein at the atomic level. It is also utilized to predict and ascertain the behavior of a ligand in the binding site of a particular protein of interest [18]. The binding affinity and orientation of some drug at a binding site have been predicted quite often with the use of this technique. In this research, we experimentally and computationally evaluated the structural properties of 4-chloro-6-phenylamino-1,3,5-Trianzin-2,4-dichlorophenylthiazol, and also the interaction of this compound with two corona virus proteins; 3TNT and 6LU7 using molecular docking.

2 Experimental and computational details

2.1 Experimental

2.1.1 Synthesis of 4-chloro-6(phenylamino)-1,3,5-triazin-2-yl)amino-4-(2,4 dichlorophenyl)thiazol-5-yl-diazenyl)phenyl

The synthesis of 4-chloro-6(phenylamino)-1,3,5-triazin-2-yl)amino-4-(2,4 dichlorophenyl)thiazol-5-yl-diazenyl)phenyl was achieved by condensing cyanuric chloride with aniline, using equimolar mixtures of initial starting materials in aqueous solution of toluene at temperature range of –10 to 50 °C. Cyanuric chloride (9.22 g, 0.05 mol) was reacted with aniline (27 g, 0.3 mol) at molar ratio of 1:6. The compound formed (2-aniline-4, 6-dichloro-1, 3, 5-triazine (0.05 mol) was later reacted with 2-amino, 4-(p-chlorophenyl) thiazole in the ratio of 1:1 at 0–5 °C for 3 h resulting in the formation of six hetero-bifunctional compounds. The schematic reaction route is reported in Figure 1.

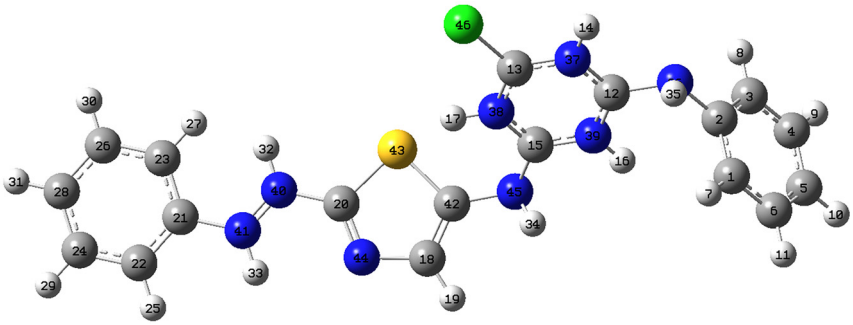

Figure 1: Optimized structure of CPTDT with atomic labelling.

2.1.2 NMR

^{1}H-NMR and ^{13}C-NMR of the investigated compound was conducted using Bruker AVANCE DPX NMR spectrometer operating at 400 and 101.6 MHz. Chloroform ($CDCl_3$) and tetramethyl silane (TMS) $(CH3)_4Si$ were utilized as solvent and internal reference standard respectively for the NMR analysis. The ^{1}H-NMR and ^{13}C-NMR spectra of CPTDT is reported in Figure S1 of the ESI.

2.2 Computational details

In this research, all the objectives were analyzed computationally with little experimental analysis for some objectives such as NMR and UV. The studied compound was optimized using Gaussian09 and GaussView 6.0.16 [19] software packages. Natural bond orbital (NBO) analysis was evaluated with the aid of NBO 3.1 software [20] embedded in GaussView 6.0.16 in order to verify the type of interaction, inter molecular charge transfer (ICT) existing within the studied compound and its stability. Geometry optimization was executed at DFT/B3LYP/6-31 + G(*d*) level of theory. The optimized structure of the studied compound with atomic labelling is presented in Figure 2. Multiwfn programme [21] was used for plotting of the spectroscopy results. The ADMET properties of the investigated compound were evaluated using PKCSM online tool kit [22]. Molecular docking of covid-19 proteins with the ligand (CPTDT) was conducted using the crystal structure of 3TNT and 6LU7 co-crystallized with CPTDT. The optimized structure of CPTDT was utilized for molecular docking analysis. Proteins used were obtained from protein data bank (PDB) database. AutoDock [23] and discovery studio visualizer [24] were employed to view the docking result while pyMOL [25] was used to build the protein-ligand complex and to visualize the binding sites.

3 Result and discussion

3.1 Quantum chemical descriptors

Relevant information on the electronic property of a compound is obtained from the molecular orbital analysis. Quantum chemical descriptors such as highest occupied molecular orbital energy (E_{HOMO}), lowest unoccupied molecular orbital energy (E_{LUMO}) and ΔE ($E_{LUMO} - E_{HOMO}$) energy gap present relevant information on the nature of reactivity and kinetic stability of a compound [26]. It is predicted that the higher the energy gap value of a particular compound, the lesser the reactivity and more stable will the compound be [27]. Table 1 shows the evaluated quantum chemical parameters of the analyzed compound. The chemical phenomenal of donating and accepting electrons by a molecule is tied to the HOMO/LUMO energy values [28]. The HOMO is

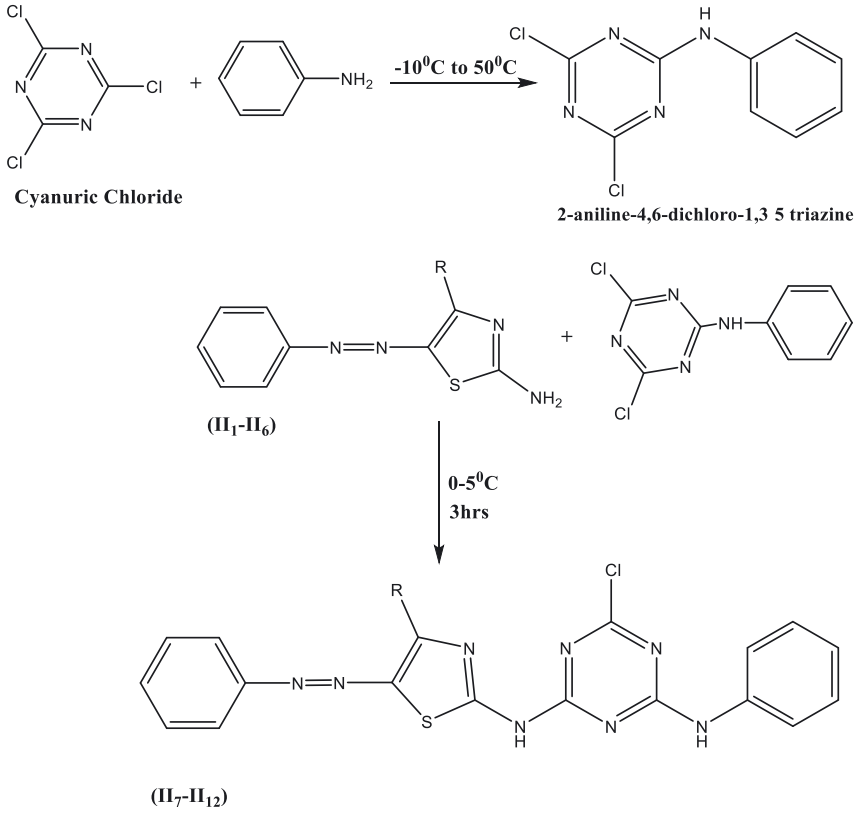

Figure 2: Reaction pathways for the studied compound.

Table 1: Calculated quantum chemical parameters of the studied compound.

Descriptors	Values
Vertical IP	6.9058 eV
Vertical EA	1.3435 eV
Mulliken electronegativity	4.1247 eV
Chemical potential	−4.1247 eV
Hardness (=fundamental gap)	5.5623 eV
Softness	0.1798 eV^{-1}
Electrophilicity index	1.5293 eV
Nucleophilicity index	3.3554 eV
HOMO	−5.7658 eV
LUMO	−2.5893 eV
Energy gap	3.1765 eV

responsible for electron donation while the LUMO accounts for electron acceptance. This implies that the higher the HOMO value, the greater the tendency of a compound to donate an electron and lower values indicate that the molecule presents a strong electron accepting property.

HOMO-LUMO of the studied compound was estimated at DFT/B3LYP/6-31 + G(d) level of theory. The calculated values are seen as thus: HOMO (–0.211891 a.u), LUMO (–0.095156 a.u), and energy gap of (0.116735 a.u). To further explain the property of HOMO-LUMO energy levels, 3D plots of HOMO and LUMO energy levels of CPTDT is depicted in Figure 3. The figure represents the positive and negative charges distributed within the compound. The red portion is positive and the green is the negative. It also suggests that the HOMO and LUMO is almost localized throughout the compound. The energy gap value confirmed that either C-N or N-N orbital are involved in HOMO and LUMO energy levels, this implies that electron donation by the HOMO energy level, or acceptance of an electron by the LUMO energy level can deteriorate the molecular skeleton framework. The HOMO-LUMO gap is where the most excitations occur, which make it the most important parameter that is considered in terms of reactivity and stability of a compound. HOMO-LUMO gap (0.116735) of the compound indicates large aromatic system, which leads to mobile π-electrons within the compound since it is easy for electrons to jump to a higher energy level. Moreover, the high mobility of the π-electron in the CPTDT system indicates that there is a greater energy distribution throughout the entire compound and as such stabilizing it.

3.2 Aromaticity index

3.2.1 PDI and PLR

Para-delocalization index (PDI) is an important parameter used to verify aromatic nature of a six-membered ring (6-MR) [29, 30]. Para linear response index (PLR) is

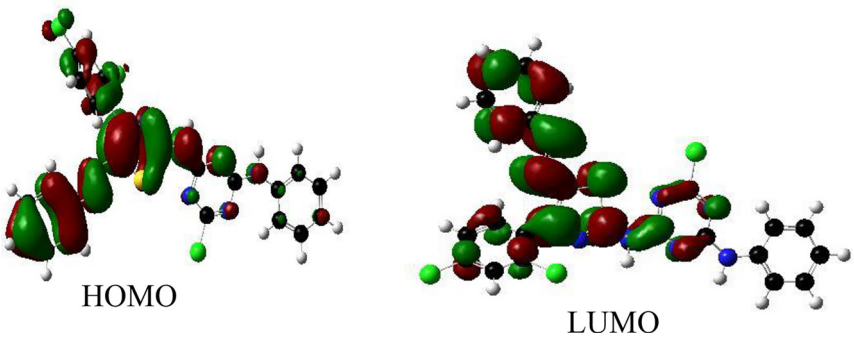

Figure 3: HOMO-LUMO plot of CPTDT.

similar to PDI, but with a slight difference. The linear relationship between PLR and PDI has been reported to be $R^2 = 0.96$ [31]. In this analysis only the 6-MR of CPTDT were considered for the PDI value. Ring three in reference to atomic ring 14–19 is considered to have a stronger aromaticity due to its high PDI value of 0.4962. The observed PDI values in the four 6-MR of the studied compound is a confirmation of the aromatic nature of the compound. Similarly, atomic ring 14–19 manifested para linear response (PLR) of 0.5979 which is the highest PLR of all the atomic rings. This also explained the more aromatic nature of atomic ring 14–19 as shown in Table 2.

3.2.2 FLU and FLU-π

Aromatic fluctuation index (FLU) is mostly implemented for investigating rings possessing any number of atoms unlike PDI which is focused on only six-membered rings [32]. FLU is defined using Eq. (1) [32–34]

$$\mathrm{FLU} = \frac{1}{n}\sum_{A-B}^{\mathrm{ring}}\left[\left(\frac{V(B)}{V(A)}\right)\left(\frac{\delta(A,B)-\delta(A,B)}{\delta(A,B)}\right)\right] \tag{1}$$

where the summation runs over all adjacent pairs of atoms around the ring, n represents the number of atoms present in the ring, σ_{ref} depicts the reference DI value. Σ is utilized in order to ensure that the ratio of atomic valences is greater than one.

While

$$\mathrm{FLU}_{\pi} = \frac{1}{n}\sum_{A-B}^{\mathrm{ring}}\left[\left(\frac{V\pi(B)}{V\pi(A)}\right)^{a}\left(\frac{\delta\pi(A,B)-\delta\mathrm{avg}}{\delta\mathrm{avg}}\right)\right]^{2} \tag{2}$$

where σ_{π} represent the average value of the DI-π for bonded atom pairs in the ring while the remaining symbols signifies that the above-mentioned parameters were estimated with the aid of π-orbitals.

However, flu-π has advantage over flu this is due to the fact that flu-π is independent on the predefined reference DI value while the main limitation of FLU is its dependence on the reference value. For both parameters, the ring with the lowest value is said to possess the strongest aromaticity which also implies more stability and less

Table 2: Aromaticity index values for the various rings in CPTDT molecule.

Atomic ring	PDI value	FLUE value	FLUE pi-	PLR	HOMA value	Bird aromaticity
1–6	0.0956	0.0092	0.0063	0.5793	0.9713	96.0288
9–13	–	0.5388	0.0093	0.5547	0.9373	96.0087
14–19	0.4962	0.0029	0.0004	0.5979	−112.29	−967.71
24–29	0.0864	0.0063	0.0021	0.5293	0.9646	94.1904
31–36	0.0910	0.0031	0.0117	0.5455	0.9619	94.7713

reactivity. Atomic ring 14–19 as shown in Table 2 has the lowest FLU and FLU-π value of 0.0029 and 0.0004 respectively which is the same ring with the highest PDI value, this correlation confirms the stronger aromaticity of atomic ring 14–19.

3.2.3 HOMA and BIRD

Table 2, highlights the HOMA and BIRD indices for each ring evident in the studied compound. HOMA is a commonly used parameter utilized for measuring aromaticity [30]. BIRD index is also a parameter that measures aromaticity of a compound with respect to geometry [33]. From the HOMA index of the investigated compound, it is obvious that none of the rings is completely non-aromantic. For instance, ring 1–6, 9–13, 24–29 and 31–36 with indices of 0.9713, 0.9372, 0.9645 and 0.9618 respectively still exhibit aromaticity since its HOMA index value does not completely correspond to a zero value [35]. However, anti-aromaticity was observed within atomic ring 14–19 due to the negative index of HOMA. For BIRD index, the closer the value is to 100, the stronger the aromaticity [36]. Thus, from the estimation, the atomic ring with BIRD value closer to 100 is atomic ring 1–6 (96.0287) followed by ring 9–13 (96.0087) with a slight difference of 0.02.

3.3 Conceptual density functional theory (CDFT)

The CDFT of the investigated compound was estimated using DFT method at B3LYP/6-31 + G(d) theory level with the aid of multiwfn software [21]. The result obtained from the CDFT of the compound under study is highlighted in Table S1 of ESI. From the computational analysis of the compound, the result revealed that the change in f^- of the studied compound is greater than zero in all the component atoms. This is a clear indication that the compound is favorable for nucleophilic attack with the exception of C15 and *N*20 with values of –0.0019 and –0.0002 respectively. This result indicates that these two positions are possible sites for electrophilic attack to take place since the two atoms have values less than zero. For relative electrophilicity (S^+/S^-) and relative nucleophilicity (S^-/S^+), atomic sites N8, N12, C6, C9, Cl20 are the most probable atomic sites susceptible to nucleophilic attack within the investigated compound. This result can be attributed to the atomic sites possessing the highest relative electrophilicity with respective values of 0.2890, 0.2734, 0.2361, 0.2246, 0.2241 as represented in the table of supporting information. More so, atomic sites H48 = 124.6627, C36 = 7.3039, C11 = 4.6823, *N*22 = 3.2754, C32 = 2.6725, C3 = 2.6636, H44 = 2.5473, *N*30 = 2.3909, C34 = 2.3516, C35 = 2.2128, H47 = 2.0223, are the sites with the highest S–/S+ ratio which makes them the most probable sites for electrophilic attack to take place.

3.4 Natural bond orbital (NBO) Analysis

Natural bond orbital (NBO) analysis is an efficient computational method utilized for comprehending intramolecular and intermolecular bonding interaction existing within a compound [37]. It also gives insight on charge transfer or hyperconjugative interaction taking place in the molecular system [38]. DFT/B3LYP/6-31G + (d) level of theory was utilized to evaluate the stabilization energy ($E^{(2)}$) of the selected compound. Stabilization energy $E^{(2)}$ of the studied compound evaluated with the aid of second order perturbation theory of the fock matix is represented in Table S2 of ESI. The higher the stabilization energy, the stronger the interaction persisting within the investigated compound. The stabilization energy $E^{(2)}$ associated with electron delocalization from the donor (i) to acceptor (j) orbital of CPTDT was estimated using Eq. (3) [37, 38].

$$E(2) = \Delta E_{i,j} = q_i \frac{F(i,j)^2}{\varepsilon_j - \varepsilon_i} \tag{3}$$

Here, q_i represent the donor orbital occupancy, ε_i and ε_j depicts the diagonal elements and F (i,j) indicates off-diagonal elements of the Fock matrix.

The intramolecular hyperconjugative interactions resulting from overlapping of bonding (σ/π) and anti-bonding (σ^*/π^*) orbitals leading to intramolecular charge transfer and stabilization in the compound is observed as π (C15–C16) to π^* (C14–C19), π (C17–C18) to π^* (C14–C19), π (C25–N29) to π^* (C24–N28) with stabilization energy of 199.35 kcal/mol, 148.33 kcal/mol, 48.40 kcal/mol respectively. Such strong interactions arise from the electronic delocalization between intermolecular ring fragments in form of resonance delocalization which is responsible for stabilizing the compound. Also, the strongest non-bonding interaction resulting from LP (3) N30 $\rightarrow\pi^*$ (C25 – *N*29) and LP (1) N22$\rightarrow\pi^*$(C26 – *N*27) gives the highest stabilization of 67.96 kcal/mol and 58.59 kcal/mol respectively. Such strong interaction aids in stabilizing the compound under study. This result offers an intuitive insight into the mechanism of stabilization, interaction, delocalization of electron within the various ring fragment and heteroatom's present in the molecule.

3.5 Atomic dipole moment corrected Hirshfeld (ADCH) charge

ADCH value of CPTDT was estimated using multiwfn software [21]. The electrostatic potential reproducibility of the CPTDT population was conducted with the aid of ADCH population charge [39]. ADCH corrected the poor electrostatic potential reproducibility challenge encountered by the Hirshfeld population which has an attribute of neglected atomic dipole moment. From the result presented in S3 of ESI, all the hydrogen atoms displayed no negative charge and also none of the correction charges of the hydrogen atoms is zero. This indicates that all the hydrogen atoms have contributed to the atomic dipole moment of the compound [40]. It was also observed from the results, that major

contributions to the atomic dipole moment originated from neighboring atoms which are mostly hydrogen. The trend of atoms possessing negative charge is displayed as thus, C14 > N22 > N27 > N13 > N28 > N29 > C32 > C17 > C2 > C34 > C33 > C36 > C1> C6 > C5 > C35 > N30 > N38 > C4 > Cl21 > Cl20 > N8 > Cl39 with corresponding values of −0.3736 > −0.3551 > −0.3399 > −0.2897 > −0.2593 > −0.1476 > −0.1342 > −0.1327 > −0.1236 > −0.1230 > −0.1213 > −0.1180 > −0.1076 > −0.1056 > −0.1036 > −0.1032 > −0.0986 > −0.0593 > 0.0530 > 0.0381 e. This result implies that these sites would be the most preferred sites for electrophilic substitution in this order of preference since some charges are more negative than others. The negative and positive charges are due to the unequal distribution of electrons in the compound by atoms due to the fact that one of the atoms is more electronegative than the other, especially the nitrogen atoms. This uneven distribution of electrons within the compound results in polarization of the atoms.

3.6 NMR analysis

NMR elucidates the structure based on paramagnetic properties of molecules and this is useful for other physicochemical properties' prediction. The paramagnetic shield is dependent on the bonded atoms. The NMR chemical shift of CPTDT was estimated with the aid of B3LYP/6-31 + G(d) GIAO method using TMS as the reference and the results are tabulated in Table 3. The corresponding theoretical NMR spectra of CPTDT is shown in Figures S1 and S2 of ESI. Experimentally, chemical shift involving the aromatic carbon atoms was recorded between 120–190 ppm in range [41], while the aliphatic carbon atoms are mostly observed behind the aromatic compounds. The results obtained from the studied compound (CPTDT), indicates that the evaluated chemical shift of the aromatic ring present in CPTDT ranges from 116.3 ppm to 165.4 ppm for C35 and C24. This correlates with the experimentally observed values at 115.9 ppm to 162.4 ppm as presented in Figure S3 of ESI. The aromatic carbon atoms bonded directly with halogen such as chlorine possesses higher chemical shifts compared to others. In the compound, the aromatic carbon atoms with the Cl atom bonded to it demonstrated a chemical shift of 165.4 ppm in C24 and it is shifted downfield which is attributed to the electron withdrawing effect of *N* and Cl attached to C24, but mostly affected by the Cl atom. Also, carbon atoms with *N* atoms experienced high chemical shift downfield as observed in C10 and C25 with the values of 147.8 ppm and 147.9 ppm respectively. However, C42 experienced a chemical shift higher than others, which could be due to the high electronegativity of the Cl atom attached to it. It can be deduced from the spectra that almost all the chemical shift falls within the aromatic region which confirms the aromatic nature of the compound (CPTDT). The once that deviated slightly might be due to the chemical effect of their neighboring atoms as observe in C6, C17, C2 with values of 116.9 ppm, 117.2 ppm and 119.8 ppm individually. In the ^{1}HNMR spectrum, the three-proton signal at 6.8 ppm is assigned to the protons on the terminal

Table 3: Experimental and Calculated ^{1}HNMR chemical shift (ppm) obtained from the investigated compound at DFT/B3LYP/6-311 + G(2d,p) GIAO method using TMS as the reference.

Atom with position	Chemical shift (ppm) TMS B3LYP/ 6-311 + G(2d,p) GIAO	Experimental chemical shift	Hydrogen atoms with positions	Chemical shift (ppm) TMS B3LYP/ 6-311 + G(2d,p)
2-C	119.7	162.4	7-H	6.9
3-C	138.1	129.9	23-H	6.4
6-C	116.9	128.5	37-H	5.4
9-C	138.1	122.6	40-H	6.8
10-C	147.7	122.3	41-H	7.1
11-C	143.6	115.9	42-H	7.4
14-C	122.3		43-H	7.1
15-C	119.5		44-H	6.0
16-C	130.2		45-H	6.8
17-C	117.1		46-H	6.6
18-C	129.8		47-H	7.0
24-C	165.3		48-H	8.2
25-C	147.9		49-H	6.7
26-C	145.9		50-H	7.0
31-C	123.3		51-H	6.6
35-C	116.2			

aromatic rings while the three-proton signal at 7.1 ppm is assigned to H41, H42, H50 which are magnetically equivalent due to long range coupling. The aromatic protons are within the range of 6.5–8.5 ppm [42]. The calculated chemical shift of the studied compound is observed between 6.03–8.2 ppm which correlates with experimental. The proton signal at 5.46 ppm is assigned to the NH proton on the ring, the standard chemical shift of the NH is expected in 3.5–4.5 ppm [43]. The shift in chemical shift at downfield is due to the strong electronegativity of the nitrogen atom.

3.7 Theoretical ADMET prediction (PKSCM)

Lipinski's rule of five (RO5) is a physicochemical parameter widely used to ascertain if a particular compound can be used as a drug [44]. According to the rule, "drug-like" molecules should exhibit; logP ≤ 5, molecular weight <500, number of hydrogen bond acceptors ≤10, and the number of hydrogen bond donors ≤5 [22]. Any molecule that violates more than one of these rules may have problem in terms of bioavailability. From the values presented in Table 4, the investigated compound was not found violating Lipinski's RO5. This implies that the compound is relatively good and may not have any problem in terms of bioavailability. ADMET properties of the investigated compound is depicted in Table 5.

Table 4: Showing the PKSCM of CPTDT.

Descriptor	Value
Molecular weight	553.866
LogP	4.8579
#Rotatable bonds	7
#Acceptors	9
#Donors	2
Surface area	224.635

Table 5: Calculated ADMET properties of CPTDT.

Model name	Predicted value	Unit
Water solubility	−3.403	Numeric (log mol/L)
Caco2 permeability	0.92	Numeric (log Papp in 10^{-6} cm/s)
Intestinal absorption(human)	100	Numeric (% absorbed)
Skin permeability	−2.735	Numeric (log kp)
Distribution		
VDss (human)	−0.324	Numeric (log L/kg)
Fraction unbound (human)	0.056	Numeric (Fu)
BBB permeability	−0.387	Numeric (log BB)
CNS permeability	−1.324	Numeric (log ps)
Metabolism		
CYP2D6 substrate	No	Categorical (Yes/No)
CYP3A4 substrate	Yes	Categorical (Yes/No
CYP1A2 inhibitor	No	Categorical (Yes/No
CYP2C19 inhibitor	Yes	Categorical (Yes/No
CYP2C9 inhibitor	Yes	Categorical (Yes/No
CYP2D6 inhibitor	No	Categorical (Yes/No Categorical (Yes/No
CYP3A4 inhibitor	No	Categorical (Yes/No
Excretion		
Total clearance	−0.179	Numeric (log mL/min/kg)
Renal OCT2 substrate	No	Categorical (Yes/No)
Toxicity		
AMES toxicity	No	Categorical (Yes/No
Max. tolerated dose (human)	0.445	Numerical (log mg/kg/day
Hepatotoxicity	No	Categorical (Yes/No
Skin sensitization	No	Categorical (Yes/No

From the ADMET result, CPTDT manifested absorbance of 100% which indicates high intestinal absorption quality of the molecule. Also, the studied compound demonstrated high water solubility value of –3.304 log mol/L. This result indicates that the compound can readily be dissolved and thus absorbed with ease in the human intestine [44]. The volume of distribution (VDss Human) of a drug reflects the total dosage of drug required to be distributed in order to give equivalent concentration of it present in blood plasma [45]. CPTDT displayed VDss value of –0.324 and thus moderate for distribution within the body. Fraction unbound (Human) suggest that the performance of a drug is dependent on the extent to which it binds to blood protein [46]. Fraction unbound for CPTDT was found to be 0.056. Blood-brain barrier (BBB) permeability of the brain prevents foreign compounds from entering freely into the brain [47]. For CPTDT, the BBB permeability (log BB) was observed to be –0.387 with an appreciating central nervous system (CNS) value (log PS) of –1.324. This result implies that the investigated compound can penetrate the brain. Cytochrome P450 inhibitors are important detoxication enzymes situated in the liver within the body [48]. CYP2C19 and CYP2C9 inhibitor are the detoxification enzymes present in the studied compound. AMES toxicity is a unique method utilized to assess mutagenicity of a compound [49]. The AMES toxicity in CPTDT is negative indicating that the compound is not mutagenic. Maximum Tolerated Dose (MTD) is the toxic dose threshold estimate of chemical present in the body [50]. The maximum tolerated dose for CPTDT was 0.445 log mg/kg/day. Hepatotoxicity signifies the amount of damage caused by a drug to the liver, and it is the primary cause of drug attrition [51]. The result revealed that CPTDT is not hepatotoxic to the liver. Skin sensitivity is a safety indicator utilized to ascertain the possibility of a compound to induce allergic reactions such as contact dermatitis [52]. The result confirmed that CPTDT is not allergic to the skin.

3.8 Molecular docking

Molecular docking was conducted using discovery studio [24] in order to investigate the interaction between the studied compound and selected two covid-19 protein (3TNT and 6LU7). The docking result of the studied compound revealed that CPTDT exhibited good interactions, with 3TNT possessing the highest binding affinity of –9.3 while that of 6LU7 was –8.8 as shown in Table S4 of ESI. It is of notice that CPTDT demonstrated four hydrogen bonds with 3TNT protein between amino acids GLN:189, GlU:166, HIS:164, PHE:140 at a distance of 5.21, 5.08, 5.90, 6.36 respectively. However, 6LU7 protein exhibited two hydrogen bonds between amino acid GLU:290 at a distance of 2.48 for the two-bond to bind to N27 to H37. Van der Waals interactions which aids in stabilizing the ligand-protein complex [53] was seen in amino acids: SER:166, GLY:143,

LEU:27, ASN:142, THR:25, MET:165 for 3TNT protein and in amino acids: GLN:127, LYS:5, ASP:197, ASN:238, THR:195, THR;199, TYR:239, GLU:288 and LEU:272 for 6LU7 protein. The compound showed two pi-sulfur bonds between MET:49, HIS:41 and the benzene ring. It can also be seen that Cys:44, CYS:145, TYR:54, ARG:188, and ASP:187 exhibited pi-donor hydrogen bond. For 3TNT protein, pi-alkyl bond was visible in amino acid LEU:141 at a distance of 4.63 while that of 6LU7 protein was observed in amino acids; LYS137, LEU:287, LUE:286 at respective distance of 5.35, 4.83, 5.21. Pi-alkyl bonds of protein 3TNT and 6LU7 is laid out in Figures 4(a) and (b) respectively. Hydrogen bond donor and acceptor of the examined proteins are visualized in the 3D-diagram as shown in Figure 5. The two proteins interacting with the ligand within their binding pocket by the amino acids are also displayed in the 3D-diagram as visible in Figure 5. The Ramachandran plot assessment used for validation of protein structures is depicted in Figure S5 of the supporting information.

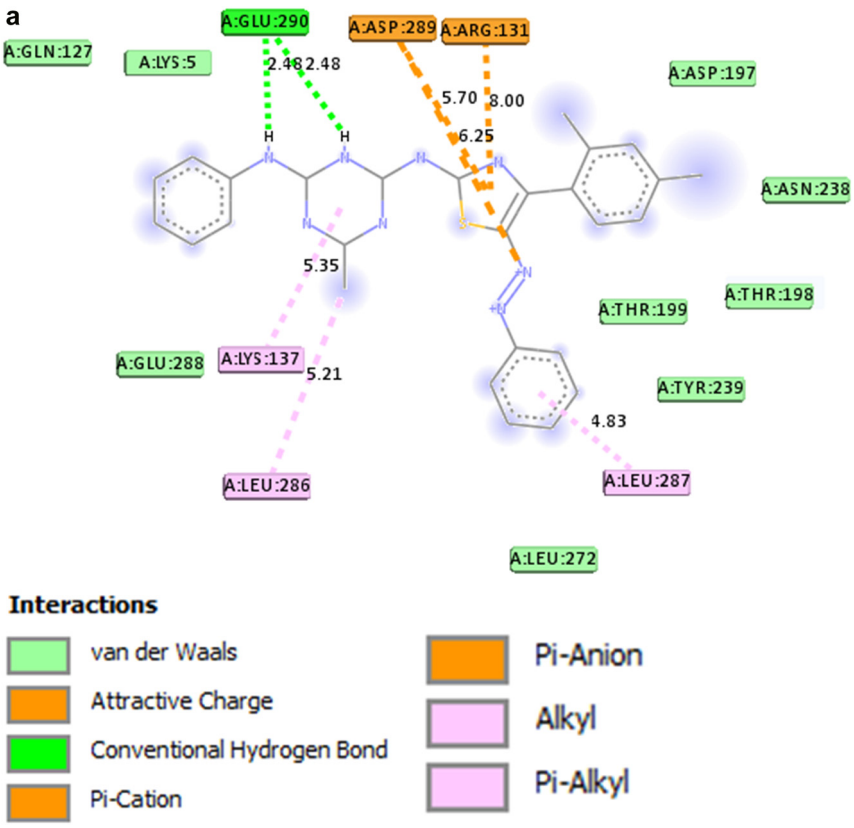

Figure 4a: 2D-diagram showing interaction of the ligand and 3TNT protein.

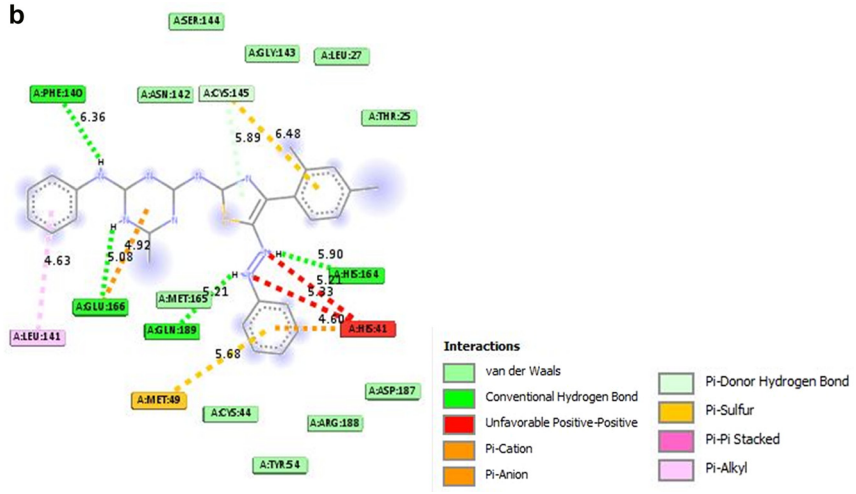

Figure 4b: 2D-diagram showing interaction of the ligand and 6LU7 protein.

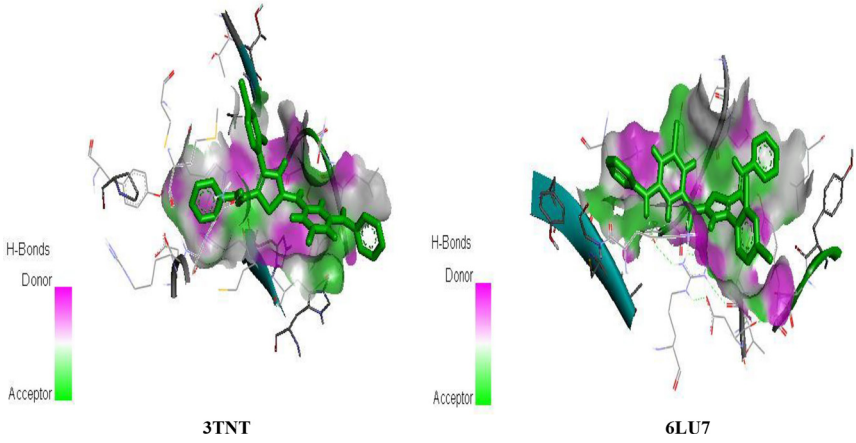

Figure 5: 3D structure of H-donor and H-acceptor of the interacted proteins.

4 Conclusions

In conclusion, we have successfully synthesized a thiazole compound named 4-chloro6(phenylamino)-1,3,5-triazin-2-yl)amino-4-(2,4-dichlorophenyl)thiazol-5-yl-diazenyl)phenyl and also performed density functional theory (DFT) calculation on the synthesized structure as a SARS-CoV-2 agent against two selected SARS-CoV-2 protein receptor namely; 3TNT and 6LU7. For the DFT calculation, geometry optimization,

HOMO-LUMO analysis, natural bond orbital (NBO) analysis of the investigated compound was conducted at B3LYP/6-31 + G(d) level of theory. HOMO–LUMO analysis revealed that the studied compound with energy gap of 0.116735 a.u exhibited better reactivity in the biological system. NBO analysis revealed that CPTDT demonstrated intramolecular hyperconjugative interactions as a result of overlapping of bonding (σ/π) and anti-bonding (σ^*/π^*) orbitals. Also, ADCH result revealed unevenly distribution of electrons between atoms in the compound which result in polarization. The NMR chemical shift exhibited theoretically by the investigated compound corresponds to its experimental value. ADMET properties of the studied compound was observed not to violate Lipinski RO5 and thus can be utilized as a drug. Moreover, the molecular docking result revealed that protein 3TNT with a high binding affinity of –9.3 in contrast to protein 6LU7 (–8.8) is the most suitable protein for ligand–protein interaction of the studied compound against covid-19.

Acknowledgement: This work did not receive any financial support from any organization. However, the authors are thankful to everyone who has contributed to the successes of this work.

Author contributions: Hitler Louis: Conceptualization, design, administration, software, and supervision, Abu S. Abu: writing-original draft, Investigation, formal analysis, and Data Curation, Ishegbe J. Eko: Formal analysis, and Methodology, Tomsmith O. Unimuke and Diana O. Odey: Investigation, Formal analysis, Validation, and writing-review & editing, Tabe N. Ntui: Writing-original draft and John A. Agwupuye: Review & editing.

Research funding: None declared.

Conflict of interest statement: The authors declare no conflicts of interest

Data Availability: All data are contained herein the supporting information and the main manuscript.

References

1. Rajagopal K, Dhandayutham S, Nandhagopal M, Narayanasamy M, Elzagheid MI, Rhyman L, et al. Thiazole derivatives: synthesis, characterization, biological and DFT studies. J Mol Struct 2022; 1255:132374.
2. Al-Otaibi JS, Mary YS, Mary YS. Theoretical insights into the solvation, electronic, chemical properties and molecular docking of some thiazole derivatives. Polycycl Aromat Comp 2022;56: 1–11.
3. Elangovan N, Thomas R, Sowrirajan S. Synthesis of Schiff base (E)-4-((2-hydroxy-3, 5-diiodobenzylidene) amino)-N-thiazole-2-yl) benzenesulfonamide with antimicrobial potential, structural features, experimental biological screening and quantum mechanical studies. J Mol Struct 2022;1250:131762.
4. Gümüş M, Yakan M, Koca İ. Recent advances of thiazole hybrids in biological applications. Future Med Chem 2019;11:1979–98.

5. Khamees HA, Mohammed YHE, Ananda S, Al-Ostoot FH, Sangappa Y, Alghamdi S, et al. Effect of o-difluoro and p-methyl substituents on the structure, optical properties and anti-inflammatory activity of phenoxy thiazole acetamide derivatives: theoretical and experimental studies. J Mol Struct 2020;1199:127024.
6. Ujan R, Mahmood HMK, Channar PA, Ejaz SA, Saeed S, Saeed A, et al. N-(5-acetyl-4-methylthiazol-2-yl) arylamide derivatives as multi-target-directed ligands: design, synthesis, biochemical evaluation and computational analysis. J Chem Sci 2022;134:1–16.
7. Kassab RM, Gomha SM, Al-Hussain SA, Dena ASA, Abdel-Aziz MM, Zaki ME, et al. Synthesis and in-silico simulation of some new bis-thiazole derivatives and their preliminary antimicrobial profile: investigation of hydrazonoyl chloride addition to hydroxy-functionalized bis-carbazones. Arab J Chem 2021;14:103396.
8. Bera P, Aher A, Brandao P, Manna SK, Bhattacharyya I, Mondal G, et al. Anticancer activity, DNA binding and docking study of M (ii)-complexes (M= Zn, Cu and Ni) derived from a new pyrazine–thiazole ligand: synthesis, structure and DFT. New J Chem 2021;45:11999–2015.
9. Sallam HH, Mohammed YHI, Al-Ostoot FH, Akhileshwari P, Sridhar MA, Khanum SA. Experimental and computational studies on the synthesis and structural characterization of 2-(4-chlorophenoxy)-N-[4-(4-methylphenyl)-1, 3-thiazol-2-yl] acetamide. J Mol Struct 2022;1249: 131588.
10. Bhoge ND, Mohite PB, Deshmukh VK, Magare BK. A comprehensive review on synthetic strategy of benzothiazole lead and pharmacological importance. Indian J Pharm Sci 2021;2:15–9.
11. Obu QS, Louis H, Odey JO, Eko IJ, Abdullahi S, Ntui TN, et al. Synthesis, spectra (FT-IR, NMR) investigations, DFT study, in silico ADMET and Molecular docking analysis of 2-amino-4-(4-aminophenyl) thiophene-3-carbonitrile as a potential anti-tubercular agent. J Mol Struct 2021; 1244:130880.
12. Abu-Melha S, Gomha SM, Abouzied AS, Edrees MM, Abo Dena AS, Muhammad ZA. Microwave-Assisted one pot three-component synthesis of novel bioactive thiazolyl-pyridazinediones as potential antimicrobial agents against antibiotic-resistant bacteria. Molecules 2021;26:4260.
13. Jaladanki CK, Khatun S, Gohlke H, Bharatam PV. Reactive metabolites from thiazole-containing drugs: quantum chemical insights into biotransformation and toxicity. Chem Res Toxicol 2021;34: 1503–17.
14. Shirani MA, Maleki MH, Asadi P, Dinari M. Benzothiazolopyridine compounds: facial synthesis, characterization, and molecular docking study on estrogen and progesterone receptors. J Mol Struct 2021;1243:130792.
15. Aldujaili RAB. Preparation and characterization of some new benzothiazole-heterocyclic derivatives. Egypt J Chem 2021;64:8–9.
16. Kubba AAM, Rahim NA. Synthesis, characterization and antimicrobial evaluation with DFT study of new two-amino-4-(4-chlorophenyl) thiazole derivatives. (P-ISSN: 1683-3597, E-ISSN: 2521-3512). Iraqi J Pharm Sci 2018;27:79–88.
17. Madni M, Ahmed MN, Hameed S, Shah SWA, Rashid U, Ayub K, et al. Synthesis, quantum chemical, in vitro acetyl cholinesterase inhibition and molecular docking studies of four new coumarin based pyrazolylthiazole nuclei. J Mol Struct 2018;1168:175–86.
18. Soltani A, Khan A, Mirzaei H, Onaq M, Javan M, Tavassoli S, et al. Improvement of anti-inflammatory and anticancer activities of poly (lactic-co-glycolic acid)-sulfasalazine microparticle via density functional theory, molecular docking and ADMET analysis. Arab J Chem 2022;15: 103464.
19. Dennington R, Keith TA, Millam JM. GaussView, Version 6. Shawnee Mission, KS: Semichem Inc.; 2016.
20. Glendening ED, Reed AE, Carpenter JE, Weinhold F. NBO, Version 3.1. Pittsburgh, PA: Gaussian. Inc.; 2003.

21. Lu T, Chen F. Multiwfn: a multifunctional wavefunction analyzer. J Comput Chem 2012;33:580–92.
22. Pires DE, Blundell TL, Ascher DB. pkCSM: predicting small-molecule pharmacokinetic and toxicity properties using graph-based signatures. J Med Chem 2015;58:4066–72.
23. Trott O, Olson AJ. AutoDock Vina: improving the speed and accuracy of docking with a new scoring function, efficient optimization, and multithreading. J Comput Chem 2010;31:455–61.
24. Jejurikar BL, Rohane SH. Drug designing in discovery studio. Asian J Res Chem 2021;14:135–8.
25. Schrödinger L, DeLano W. PyMOL; 2020. Available from http://www.pymol.org/pymol.
26. Janani S, Rajagopal H, Muthu S, Aayisha S, Raja M. Molecular structure, spectroscopic (FT-IR, FT-Raman, NMR), HOMO-LUMO, chemical reactivity, AIM, ELF, LOL and Molecular docking studies on 1-Benzyl-4-(N-Boc-amino) piperidine. J Mol Struct 2021;1230:129657.
27. Vasanthakumari R, Nirmala W, Sagadevan S, Mugeshini S, Rajeswari N, Balu R, et al. Synthesis, growth, crystal structure, vibrational, DFT and HOMO, LUMO analysis on protonated molecule-4-aminopyridinium nicotinate. J Mol Struct 2021;1239:130449.
28. Basha F, Khan FLA, Muthu S, Raja M. Computational evaluation on molecular structure (Monomer, Dimer), RDG, ELF, electronic (HOMO-LUMO, MEP) properties, and spectroscopic profiling of 8-Quinolinesulfonamide with molecular docking studies. Comput Theor Chem 2021;1198:113169.
29. Karimi P, Sanchooli M, Shoja-Hormozzahi F. Estimation of resonance assisted hydrogen bond (RAHB) energies using properties of ring critical points in some dihydrogen-bonded complexes. J Mol Struct 2021;1242:130710.
30. Molavian MR, Abdolmaleki A, Eskandari K. Strain or electronic effects? MP2 and DFT aromaticity investigation in small ring annulated benzene. Comput Theor Chem 2017;1099:102–8.
31. Vu KB, Nhi TLP, Vu VV, Ngo ST. How do magnetic, structural, and electronic criteria of aromaticity relate to HOMO–LUMO gap? An evaluation for graphene quantum dot and its derivatives. Chem Phys 2020;539:110951.
32. Sablon N, De Proft F, Solà M, Geerlings P. The linear response kernel of conceptual DFT as a measure of aromaticity. Phys Chem Chem Phys 2012;14:3960–7.
33. Edim MM, Enudi OC, Asuquo BB, Louis H, Bisong EA, Agwupuye JA, et al. Aromaticity indices, electronic structural properties, and fuzzy atomic space investigations of naphthalene and its aza-derivatives. Heliyon 2021;7:e06138.
34. Kores JJ, Danish IA, Sasitha T, Stuart JG, Pushpam EJ, Jebaraj JW. Spectral, NBO, NLO, NCI, aromaticity and charge transfer analyses of anthracene-9, 10-dicarboxaldehyde by DFT. Heliyon 2021;7:e08377.
35. Báez-Grez R, Arrué L, Pino-Rios R. Quantitative analysis of aromaticity in azines by means of dissected descriptors based on the magnetic criteria. Chem Phys Lett 2021;781:138973.
36. Świderski G, Kalinowska M, Jabłońska-Trypuć A, Wołejko E, Wydro U, Łyszczek R, et al. Studies on the relationship between the structure of pyrimidinecarboxylic, pyridazinecarboxylic and pyrazinecarboxylic acids and their antimicrobial and cytotoxic activity. J Mol Struct 2021;1231: 129903.
37. Agwupuye JA, Neji PA, Louis H, Odey JO, Unimuke TO, Bisiong EA, et al. Investigation on electronic structure, vibrational spectra, NBO analysis, and molecular docking studies of aflatoxins and selected emerging mycotoxins against wild-type androgen receptor. Heliyon 2021;7:e07544.
38. Bisong EA, Louis H, Unimuke TO, Odey JO, Ubana EI, Edim MM, et al. Vibrational, electronic, spectroscopic properties, and NBO analysis of p-xylene, 3, 6-difluoro-p-xylene, 3, 6-dichloro-p-xylene and 3, 6-dibromo-pxylene: DFT study. Heliyon 2020;6:e05783.
39. Ferino-Pérez A, Vélayoudom FL, Belia L, Glaude EL, Gaspard S, Jáuregui-Haza UJ. In silico development of new PET radiopharmaceuticals from mTOR inhibitors. J Mol Graph Model 2022;111: 108057.

40. Carmona-Espíndola J, Núñez-Rojas E, García-Melgarejo V, Gázquez JL, Alejandre J. Constrained dipole moment density functional theory for charge distributions in force fields for the study of molecular fluids. J Chem Phys 2020;152:124116.
41. Ware SA, Hartman BE, Waggoner DC, Vaughn DR, Bianchi TS, Hatcher PG. Molecular evidence for the export of terrigenous organic matter to the north Gulf of Mexico by solid-state 13C NMR and Fourier transform ion cyclotron resonance mass spectrometry of humic acids. Geochem Cosmochim Acta 2022;317:39–52.
42. Wang Z, Ma Q, Huang X, Zhang T, Shao J, Zhang X, et al. S/Se-embedded acenaphthylene-imide-containing polycyclic heteroaromatic hydrocarbon. Chin Chem Lett 2022;33:271–5.
43. Faihan AS, Hatshan MR, Alqahtani AS, Nasr FA, Al-Jibori SA, Al-Janabi AS. New divalent metal ion complexes with 1, 8-diaminonapthalene-2-thione: synthesis, Spectroscopic, anti-bacterial and anticancer activity studies. J Mol Struct 2022;1247:131291.
44. Chen X, Li H, Tian L, Li Q, Luo J, Zhang Y. Analysis of the physicochemical properties of acaricides based on Lipinski's rule of five. J Comput Biol 2020;27:1397–406.
45. Savva M. On the origin of the apparent volume of distribution and its significance in pharmacokinetics. J Biosci Med 2022;10:78–98.
46. Farrar JE, Mueller SW, Stevens V, Kiser TH, Taleb S, Reynolds PM. Correlation of antimicrobial fraction unbound and sieving coefficient in critically ill patients on continuous renal replacement therapy: a systematic review. J Antimicrob Chemother 2022;77:310–9.
47. Meng Q, Meng H, Pan Y, Liu J, Li J, Qi Y, et al. Influence of nanoparticle size on blood–brain barrier penetration and the accumulation of anti-seizure medicines in the brain. J Mater Chem B 2022;10: 271–81.
48. Gaedigk A, Boone EC, Scherer SE, Lee SB, Numanagić I, Sahinalp C, et al. CYP2C8, CYP2C9 and CYP2C19 characterization using next generation sequencing and haplotype analysis: a GeT-RM collaborative project. J Mol Diagn 2022;24:337–50.
49. Fan Y, Fu Y, Zhou Y, Liu Y, Hao B, Shang R. Acute, subacute oral toxicity and Ames test of Py-mulin: an antibacterial drug candidate. BMC Pharmacol Toxicol 2022;23:1–12.
50. Bennett RP, Postnikova EN, Eaton BP, Cai Y, Yu S, Smith CO, et al. Sangivamycin is highly effective against SARS-CoV-2 in vitro and has favorable drug properties. JCI insight 2022;7. https://doi.org/10.1172/jci.insight.153165.
51. Balkrishna A, Bhattacharya K, Sinha S, Dev R, Srivastava J, Singh P, et al. Apparent hepatotoxicity of Giloy (Tinospora cordifolia): far from what meets the eyes. J Clin Exp Hepatol 2022;12:239–40.
52. Temiz SA, Abdelmaksoud A, Wollina U, Kutlu O, Dursun R, Patil A, et al. Cutaneous and Allergic reactions due to COVID-19 vaccinations: a review. J Cosmet Dermatol 2022;21:4–12.
53. Gurung AB, Ali MA, Lee J, Farah MA, Al-Anazi KM, Al-Hemaid F. Artesunate induces substantial topological alterations in the SARS-CoV-2 Nsp1 protein structure. J King Saud Univ Sci 2022;3: 101810.

Supplementary Material: The online version of this article offers supplementary material (https://doi.org/10.1515/psr-2021-0161).